Enhanced crystal stability in a binary mixture of charged colloidal spheres

Patrick Wette,[1,*] Hans Joachim Schöpe,[2,*] and Thomas Palberg[2]
[1]*Institut für Materialphysik im Weltraum, Deutsches Zentrum für Luft- und Raumfahrt, 51170 Köln, Germany*
[2]*Institut für Physik, Johannes Gutenberg-Universität Mainz, Staudinger Weg 7, 55128 Mainz, Germany*
(Received 1 April 2009; revised manuscript received 25 June 2009; published 27 August 2009)

We report on the phase behavior of a binary charged sphere mixture of size ratio $\Gamma=0.68$ and charge ratio $\Lambda\approx 1$ as a function of composition p and number density n. For $p=0.1-0.3$ we observe freezing at densities well below the freezing densities of the pure components. At all compositions our data indicate the formation of substitutional alloy crystals of body centered cubic structure. No indications for compound formation were observed. Rather, our findings point at the first observation of an upper azeotrope. Measurements of the crystallization kinetics reveal a combined density and composition dependence of growth velocities and nucleation rate densities, with small but significant anomalies at $p^*=0.2$. These correlated deviations can be rationalized within classical theories of solidification and suggest an increased similarity between melt and solid for this particular composition.

DOI: 10.1103/PhysRevE.80.021407 PACS number(s): 82.70.Dd, 81.10.−h, 64.60.Q−

I. INTRODUCTION

The phase behavior of colloidal spheres in general and the formation of colloidal crystals in particular has been studied extensively for several decades. Investigations include hard spheres, charged spheres and entropically attractive systems [1–3] and are guided by valuable instrumental [4–6] and theoretical [7,8] developments. While much is already known about one-component crystals formed for different interaction types and strengths, binary colloidal crystals have been investigated mainly in hard sphere or near hard sphere systems. Their first observations of colloidal compound crystals were made in natural gem opals [9,10]. Shortly after first observations in sedimented synthetic bead systems followed [11]. Chaikin and co-workers presented first systematic studies on the elasticity and diffusivity in substitutional alloys formed under de-ionized conditions from charged spheres [12]. The first phase diagrams were obtained for hard spheres, showing compound formation and large regions of amorphous solids [13–18]. Very similar in their phase diagram are charged spheres at large number densities, where the repulsive Coulomb interaction is strongly screened by the sphere counterions [11]. Recent work shows that compound formation and vitrification also dominate the phase behavior in the nanocolloidal domain [19]. Early theoretical treatment assumed immiscible spheres, leading to the formation of a eutectic phase diagram [20]. However, both cell model calculations and simulations evidenced finite miscibility and therefore dominance of compound formation of AB for $\Gamma<0.45$, and AB_2 and AB_{13} type for $\Gamma<0.62$ [21–24]. Here the size ratio $\Gamma=a_S/a_L$ is defined in terms of the radii of the small (S) and large (L) component. Up to $\Gamma\approx 0.8$, eutectic behavior under formation of A and B crystals with small dissolved amounts of the other component is expected. For still larger values of Γ formation of substitutional crystals with either lower azeotrope or spindle type phase diagrams is anticipated [25]. The formation of amorphous solids is either attributed to the closeness of freezing and glass transition or the influence of polydispersity [26]. Also kinetic aspects may play a decisive role. While colloidal crystallization in one component systems in general is found to follow the classical nucleation theory [5,27], the formation of crystal nuclei from their binary melts shows a strong dependence on the type of phase diagram present and may influence the phase selection [25].

By contrast to hard spheres, charge spheres at moderate to low screening show much less pronounced compound formation. Already early work had shown that either at large size ratio substitutional crystals prevail [12,28], or at small size ratio the system phase separates [29,30]. Observation of compounds seems to be aided by sedimentational compression [31] and restricted to densities well above the freezing density $n_F(p)$ [32,33], where the composition $p=n_S/(n_S+n_L)$ is defined in terms of the number densities n of pure components. The types of phase diagrams observable range from spindle to lower azeotrope (both with formation of substitutional alloys in the solid phase) to eutectics (with or without mutual solubility of the two coexisting crystal phases) [34,35]. At elevated salt concentrations and/or sufficiently large polydispersity again extended amorphous regions are observed in the phase diagrams of the latter two types [34]. The first extended studies, covering a somewhat broader range of size ratios and compositions and combining determination of phase transition points with measurements of other properties were presented by [36]. A set of detailed studies combining investigations of elasticity, diffusivity, conductivity, and crystallization kinetics is available for substitutional alloys [37–39] presenting spindle type phase diagrams [40]. Very recently we have given a review on the types of phase diagrams obtainable in exhaustively deionized mixtures of different size and charge ratios as a function of number density and composition [41].

All mixtures investigated so far (including both hard and charged spheres) showed a suppression of crystal stability, i.e., the melting line is shifted toward larger number densities $n_M(p)$ for compositions $0<p<1$. In the present paper we investigate a mixture, where the size ratio $\Gamma=0.68$ is significantly smaller than the effective charge ratio $\Lambda\cong 1$. Interest-

*Corresponding author

TABLE I. Particle and suspension properties of the two employed species of de-ionized charged sphere suspensions: $2a$: nominal diameter according to dynamic light scattering (DLS) measurements, N: titrated negatively charged surface group number; $Z_{eff,\sigma}$: effective charges from conductivity; $Z_{eff,G}$: effective charges from elasticity; n_F and n_M: freezing and melting densities of the pure components as observed using the continuous conditioning technique.

Sample	Source	2a [nm]	N	$Z_{eff,\sigma}$	$Z_{eff,G}$	n_F (μm^{-3})	n_M (μm^{-3})
PnBAPS68	BASF	68(DLS)	1435	450 ± 16	331 ± 3	6.1 ± 0.2	6.2 ± 0.2
PS100B	BangsLab.	100(DLS)	49900	530 ± 38	327 ± 10	3.8 ± 0.5	4.5 ± 0.2
Ratio		0.68	0.03	0.84	1.01		

ingly, we find a narrow composition range $p^*=0.1-0.3$ of pronouncedly enhanced crystal stability. The melting density $n_M(p^*)$ is even below the melting density of the pure components. In principle, this may be caused both by compound formation or by the occurrence of an upper aceotrope [42]. We therefore performed further systematic and very sensitive measurements of the system structure, the elasticity the conductivity and the kinetics of crystal nucleation and growth. We observe small but significant deviations from the behavior expected for substitutional crystals formed in a spindle type phase diagram. Their smallness excludes the formation of a compound. They are, however, correlated with the specific phase diagram shape observed. In combination with the latter our data on the other system properties provide indirect evidence of an enhanced miscibility of the particles in crystalline phase, but also seems to suggest a prestructuring of the melt.

In the following we shall first shortly introduce the employed system and its preparation and recall the most important features of the different experimental techniques. We then shall present the data collected in the different systematic experiments. We continue with their interpretation and a discussion of their interrelation. We conclude with a more general interpretation of our observation in view of previously obtained phase diagram types.

II. EXPERIMENTAL

A. Samples and sample conditioning

Colloidal crystals were prepared from aqueous suspensions of two species of charged colloidal spheres. *PS100B* are commercially available, carboxyl-modified polystyrene latex spheres (Bangs-Laboratories, Fishers, USA; Lot No. 3067), *PnBAPS68* are poly-n-butylacrylamid-polystyrene copolymer spheres, stabilized by sulfate groups (BASF AG, Ludwigshafen, Germany, Laboratory Code 2168/7387). In an aqueous environment the particles charged up negatively due to the dissociation of the end groups following either the reaction: $-\mathrm{COOH}\rightarrow-\mathrm{COO}^-+\mathrm{H}^+$ in case of carboxyl end groups or $-\mathrm{SO_4H}\rightarrow-\mathrm{SO_4^-}+\mathrm{H}^+$ in case of sulfate end groups. The absolute number of carboxyl, respectively, sulfate groups N was determined via conductometric titration with sodium hydroxide (NaOH). Both species were carefully characterized as de-ionized single component suspensions. A compilation of results is given in Table I. The size ratio of the binary mixture is $\Gamma=0.68$. The table lists two effective charges. The interested reader may find a discussion of the interesting physics underlying these two quantities in [43,44], of their theoretical modeling in [45–48], and of experimental observations in [49–51]. In short, the conductivity effective charge relates to the concentration of counterions and is here used to control the state of conditioning. The elasticity effective charge relates to the derivatives of the interaction potential at the nearest-neighbor distance. It thus depends on the interaction strength and range and governs the phase behavior [52]. For our mixtures the corresponding effective charge ratio is $\Lambda\cong1$. Furthermore we refer the interested reader to electrophoretic mobility data in one of our previous publications [53].

Still, due to the larger particle size *PS100B* crystallizes at slightly lower number density than *PnBAPS68*. The crystallization of *PnBAPS68* and *PS100B* can be investigated in a particle number density range (volume fraction range) of $n=6.1-65$ μm^{-3} ($\Phi=0.001-0.011$) and $n=3.8-55$ μm^{-3} ($\Phi=0.002-0.029$), respectively. Corresponding lattice constants can be determined within the range between $g=314-689$ nm for the *PnBAPS68* and in the range $g=331-806$ nm for the *PS100B* system. The lower bound is determined by the freezing point of the individual particle species and the upper bound is due to the increasing turbidity of the samples and the onset of multiple scattering events. These ranges do overlap over a wide concentration range, so that mixtures of the two species can be investigated within the overlapping region. Note, that both species show a narrow coexistence region.

Pure component samples and mixtures were prepared from precleaned stock suspensions of known volume fractions around 0.1. These were mixed according to the desired composition $p=p_{68}=n_{68}/(n_{68}+n_{100})$ and filled into a peristaltically driven closed conditioning circuit. Technical details of this continuous conditioning method as well as the characterization of its performance are given elsewhere [38]. In short, the Teflon®-tubings of the circuit connect an ion exchange chamber, a reservoir under an inert Ar atmosphere (to add milli-q-grade water for dilution), and a set of different measurement cells: for static light scattering cylindrical cells of 10 mm diameter, for reflection spectroscopy rectangular cells of 10×10 mm^2 while for microscopy flat rectangular cells of 10×2 mm^2 cross section were used. All cell types are made of quartz glass. Hence, different experiments can be performed in parallel at identical conditions without the

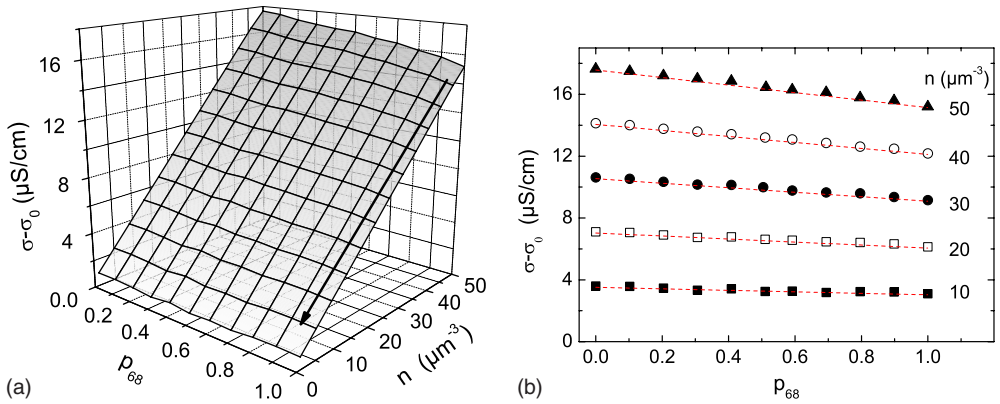

FIG. 1. (Color online) a) 3D plot of the background corrected low frequency conductivity σ of the binary mixture PnBAPS68/PS100B in dependence on particle number density n and number fraction p_{68} of PnBAPS68. The arrow marks the direction of dilution of the system. Every crossing point in the wire gauze of the shown conductivity surface represents a data point. (b) Fits of Eq. (1) to data for representative number densities (dashed lines). At all particle number densities the conductivity varies linearly with the composition and is well described within the extension of Hessinger´s model to binary mixtures [38].

need to transfer the fragile sample from one setup to another. Static light scattering was used to control the adjusted number density, while conductivity was used to determine the composition of de-ionized mixtures at known n.

B. Number density control

Static light scattering measures the intensity of scattered light $I(q)$ as a function of scattering vector q of magnitude $q=(4\pi\nu/\lambda)\sin(\Theta/2)$, where ν is the refractive index of the suspension, λ the wavelength of the light in vacuum and Θ the scattering angle. The position of the Bragg peaks q_{hkl} relate to the crystal structure and the lattice constant g of the crystals as $q_{hkl}=(2\pi/g)(h^2+k^2+l^2)^{1/2}$, where h,k,l are the Miller indices [1,2]. Using $n_{\mathrm{bcc}}=2/g^3$ the number density is obtained. Measurements were performed in a Debye Scherrer geometry with powder averaging by sample rotation about the vertical axis [54]. Relative uncertainties in n are on the order of 1–2 %.

C. Composition control

Conductivity experiments were conducted at frequencies of $\omega=400$ Hz (electrode LR325/01 with bridge LF538, WTW, Germany). This frequency is low enough to measure the dc limit of conductivity but large enough to inhibit significant electrophoretic particle transport. The relative uncertainty of an individual measurement at known n amounts to 2% with the main contribution coming from the unknown residual ion concentration. The particle number density dependence of σ was observed to be strictly linear for the de-ionized pure component suspensions. These data are well described by the independent ion migration model of Hessinger *et al.* [55]: $\sigma-\sigma_0=neZ_{eff,\sigma}(\mu_P+\mu_H^+)$, where e is the elementary charge and σ_0 is the background conductivity stemming from the self-dissociation of water. μ_P and $\mu_{\mathrm{H+}}$ denote the mobilities of particles and counterions. $Z_{eff,\sigma}$ denotes the effectively transported charge of the particles, which is equivalent to the number of freely moving counterions. Measuring n by static light scattering a calibration curve can be established, from which the effectively transported charge is inferred for a single component system. An extension of this model for thoroughly de-ionized binary mixtures was given by Wette *et al.* [38]. The expression reads

$$\sigma-\sigma_0=ne[pZ_{eff,\sigma,S}(\mu_S+\mu_H^+)+(1-p)Z_{eff,\sigma,L}(\mu_L+\mu_H^+)]. \quad (1)$$

Here, μ_S and μ_L are the small and large particle mobilities. Both the original model and its extension have successfully been checked for one component systems, fluid mixtures, and solid solutions at $\Gamma\geq 0.85$ to hold irrespectively of the suspension structure, concentration, temperature and composition [38,55,56].

Since the applicability of Eq. (1) is essential in preparation control, we show the test of this model for the present mixture in Figs. 1(a) and 1(b). Composition was varied in steps of 0.1 in p, the number density was varied between $n=10$ $\mu\mathrm{m}^{-3}$ and to $n=50$ $\mu\mathrm{m}^{-3}$ in steps of 5 $\mu\mathrm{m}^{-3}$. The black arrow shows in the direction of consecutive dilution with solvent between individual measurements. The conductivity values form a flat plane over the p-n-coordinates representing a linear behavior in dependence on both quantities.

Figure 1(b) compares the composition dependence for five representative n to the expectations of Eq. (1). The shown small residual deviations are nonaveraged. They represent the combined uncertainties in the adjustment of interaction parameters n, p_{68} and c, the residual salt concentration of individual experiments. As can be seen the deviations are indeed very small and show a reliable sample preparation. Hence, within continuous de-ionization, we are able to control the number density via static light scattering and the composition via conductivity. At the same time we can also monitor the progress of de-ionization from the development of conductivity in time. In fact, within a few hours the conductivity drops to a stationary low value, which corresponds to residual ionic impurities on the level of the self-dissociation of water.

D. Morphology control

During conditioning the sample flows through the optical cell and is retained in a shear molten state. When the flow is stopped, it readily solidifies. The observable morphology results from the competition between different solidification scenarios, depending strongly on the interaction strength and range, which determines the "undercooling" of the shear melt. At low undercooling, i.e., in the vicinity of the freezing transition, the nucleation rate density is quite low and the solidification process is dominated by crystal growth. Heterogeneous nucleation at the container walls competes with homogeneous nucleation in the sample center and is dominating the nucleation process. With increased undercooling the homogeneous nucleation rate increases rapidly and at densities well above n_F heterogeneous nucleation is suppressed, solidification becomes dominated by homogeneous nucleation leading to isotropic polycrystalline solids.

Further, thin flat walled cells favors wall crystal formation, while in the case of cylindrical cells, wall crystal growth is frustrated. Finally, the formerly applied shear exerts an orienting influence on the shear melt close to the cell walls, which leads to the formation of oriented wall crystals. For further details on the resulting morphologies the interested reader is referred to [57,58].

In the present paper we employ these means to obtain different solidification scenarios and thus those sample morphologies, which were most suitable for the respective experiments. For instance, the phase behavior was studied in flat flow cells of rectangular cross section, providing a suitable nucleation site at their walls and thus allowing to reach equilibrated states in coexistence. It was regularly employed for the growth velocity studies, as it provides wall crystals with planar crystal melt interfaces [59]. On the other side, polycrystalline material with random orientation of the grains is a necessary pre-requisite for static light scattering using a Debye-Scherrer technique, as well as for the determination of the shear modulus. In the latter case the presence of (oriented) wall crystals is known to significantly influence the results [60]. We therefore used cylindrical cells for these latter measurements. At low n oriented wall nucleated crystals as well as homogeneous nucleated crystals were observed, while homogeneous nucleated polycrystalline material prevails for $n \geq 15\ \mu\mathrm{m}^{-3}$.

E. Phase behavior

Microscopy is well suited to locate the melting and freezing lines of our mixtures in the n-p diagram. Here the suspension is investigated in flat rectangular sample cells and shear oriented wall crystals can be prepared allowing a high precise determination of the phase boundaries. Close to freezing the suspension is observed between crossed polarizers. Disordered regions appear black, while crystalline regions appear in bright colors corresponding to those of the polarized Bragg diffraction from the sample [61]. Close to melting Bragg microscopy is applied [5]. The sample is illuminated under an angle Θ with respect to the optical axis of the microscope. If Θ fulfils the Bragg condition the crystallite appears bright, while the remaining sample appears dark. We here use contrast inversion [59] by choosing an illumination angle slightly off the 110 reflection. This allows excellent discrimination of small volumes of remaining melt. Identification of the crystal structure employed static light scattering using cylindrical sample cells and by reflection spectroscopy using large rectangular cells, where homogeneous nucleation in the bulk dominates the solidification. For compounds the compositional order would be reflected by the appearance of additional peaks at q smaller than the scattering vector of the principal peak.

F. Elasticity measurements

Elasticity was measured using torsional resonance spectroscopy (TRS), a nondestructive optical method. It derives the shear modulus G from the resonance frequencies of small amplitude torsional vibrations excited about the vertical axes of our samples contained in cylindrical vials. A description of the technical details has been given elsewhere [54]. This technique was used to determine the shear elasticity and the elasticity effective charges of the pure components [49]. For a polycrystalline solid of body centered cubic (bcc) structure G is connected to the pair energy of interaction at the nearest neighbor distance $V(d)$,

$$G_{\mathrm{bcc}} = f\frac{4}{9}nV(d)\kappa^2 d^2 \tag{2}$$

with the factor 4/9 accounting for a bcc structure with a nearest neighbor distance of $d=\sqrt{3}/\sqrt[3]{4n}$. $f=0.5$ is an empirical factor accounting for the orientation average in a polycrystalline material [62–64]. The interaction between charged spheres in a mixture at finite concentration is not known exactly. Although first attempts have been made to study counterion condensation in mixtures [65], due to the presence of many body effects the applicability of effective Yukawa potentials has been generally questioned [66]. For the case of substitutional alloys, Lindsay and Chaikin have given an estimate of the composition dependence of the pair interaction energy [12]. Here the suspension is modeled as an effective one component suspension with a number weighted average effective charge, calculated from the values of the pure small and large species,

$$V(r) = k_B T \lambda_B [p^2 \tilde{Z}_S^2 + 2p(1-p)\tilde{Z}_S\tilde{Z}_L + (1-p)^2\tilde{Z}_L^2]\frac{\exp(-\kappa r)}{r} \tag{3}$$

with the thermal energy k_BT, the Bjerrum length $\lambda_B = e^2/4\pi\varepsilon_r\varepsilon_0 k_B T = 7.2$ nm in water, and

$$\tilde{Z}_i = Z_{eff,G,i}\frac{\exp(\kappa a_i)}{1+\kappa a_i}, \tag{4}$$

where the indices $i \in \{S,L\}$ again refer to the small and large species. The screening constant κ sums over the contributions of the counterions of both species and of added electrolyte of density n_{salt},

$$\kappa = \sqrt{4\pi\lambda_B\{n[pZ_{eff,G,S} + (1-p)Z_{eff,G,L}] + n_{salt}\}}. \quad (5)$$

Following [28], and using Eqs. (3)–(5) in Eq. (2) one obtains a prediction for the number weighted average shear modulus for a compositionally disordered, polycrystalline bcc solid. This five parameter modeling employs two effective charges, the particle number density, the composition, and the concentration of added salt. In our case the latter parameter is zero, while the charge parameters are assumed fixed at the values determined in independent measurements on the pure species. We are left with two experimentally variable parameters n and p. For typical values of charges, the composition dependence is nearly linear. This description of elasticity was successfully applied to the results of shear modulus measurements of substitutional alloys formed at large size ratio [28,37,39]. In general, G reacts strongly to any changes of structure or morphology [57]. Significant deviations from Eq. (2) therefore are a sensitive check for compound formation [32,33].

G. Crystallization kinetics

During preparation the sample is shear molten by continued cycling through the conditioning circuit. If the equilibrium state is solid, the sample readily solidifies after cessation of shear. For exact measurement of the crystal growth velocity shear oriented wall crystals in rectangular cells were prepared and studied by video microscopy in the Bragg or polarization mode. The dependence of the growth velocity on n and p is modeled by a Wilson-Frenkel law (WF law) for reaction controlled growth [5,67],

$$v = v_\infty\left[1 - \exp\left(-\frac{\Delta\mu}{k_BT}\right)\right]. \quad (6)$$

Here $\Delta\mu/k_BT$ is the dimensionless under cooling, with $\Delta\mu$ denoting the difference in chemical potential between melt and solid and k_BT being the thermal energy. The limiting growth velocity v_∞ corresponds to infinite under cooling. A simple estimate for $\Delta\mu$ was already given in the pioneering work of Aastuen *et al.* [67] using the difference of the particle number density in the melt to that at the phase boundary. We here follow later work of Würth *et al.*, and use $\Delta\mu = B\Pi^*$ with the reduced energy density difference $\Pi^* = (\Pi - \Pi_F)/\Pi_F$. $\Pi = \alpha n V(r)$ with the effective number of nearest neighbors denoted α. Π refers to the melt and Π_F to the coexisting fluid at freezing. The system specific proportionality constant B is obtained from fits of the WF law to experimental velocity data plotted versus Π^*. This description accounts for changes of the interaction potential through variations in the interaction parameters n, c, and Z^*. Using Eq. (4) for $V(r)$ it is readily extended to binary mixtures of compositional disorder. The approach performs well for single component systems [59] as well as for binary mixtures as long as the limiting velocity shows a linear variation with composition [68].

In the present study we measured the extension of wall nucleated crystals at different times after cessation of shear in the pumping circuit. Growth velocities were inferred as slopes in plots of the measured extension versus elapsed time. Growth was studied at $p_{68} \in \{0.0; 0.20; 0.50; 0.75; 1.0\}$ in dependence on n. Above coexistence growth was linear in time for all samples. For each set of parameters five to ten individual measurements were averaged. Depending on p measurements of the growth velocity could here be performed for densities up to 10–20 μm^{-3}. Above homogeneous nucleation interfered too strongly.

The homogeneous nucleation kinetics in the bulk were inferred from static light scattering data on solidified samples at elevated n detecting the scattering signal from the sample center using cylindrical cells. The full width at half height of the Bragg peaks Δq is related to the average size of the crystallites as $L = 2\pi K/\Delta q$, where K is the Scherrer constant for crystallites modeled as cubes of side length L [69]. For each number density and composition investigated the average of five individual measurements was taken. Relative uncertainties in L are below 20% for crystallite sizes below 50 μm corresponding to number densities $n \geq 20$ μm^{-3}. At smaller densities crystallite sizes were too large for good statistics.

The average crystallite size is governed by the competition between crystal growth and crystal nucleation during the solidification process. This is quantitatively modeled in Avrami´s model of solidification [70], relating the stationary homogeneous nucleation rate density J to the stationary crystal growth velocity v and the crystallite density $\rho = L^{-3}$ by $J = 1.158 v \rho^{4/3}$. Working at $n \gg n_F$, v is approximated by v_∞. Nucleation rate densities estimated this way carry an uncertainty of about a factor of two.

III. RESULTS

A. Phase behavior and morphology

The melting and freezing lines of our mixture are shown in Fig. 2. Interestingly for all mixtures the freezing particle number densities are below the straight connection between the pure components. With increasing p a general increase of n_F is observed, which is nonmonotonous: between $p=0.1$ and $p=0.3$ a rather sharp feature is observed where n_F is significantly lowered. The melting line runs approximately parallel to the freezing line giving a coexistence region of nearly constant width above $p=0.1$. At $p^*=0.2$ the freezing density $n_F(p^*)=2.7$ μm^{-3} and the melting density $n_M(p^*)=3.1$ μm^{-3} is even below the freezing densities of both pure components $n_{F,100}=3.8$ μm^{-3} and $n_{F,68}=6.2$ μm^{-3}.

Exemplary static light scattering patterns are shown in Fig. 3 for different compositions $n=30$ μm^{-3}. The principal peaks can be attributed to a bcc structure for all investigated samples. Particular care was given to record also the low q regions. However, no prepeaks are observed and thus no long-ranged compound or superstructure formation is discernible. One may consider phase segregation in the used mixture. If the colloidal polycrystal would consist of crystal grains only made of particles *PnBAPS68* or *PS100B*, the melting number density of this material would be higher than the straight connection between the melting number densities of the pure components. In the melt the particles would have to be mixed again due to entropic reasons and the energy costs of this mixing process would increase the melting

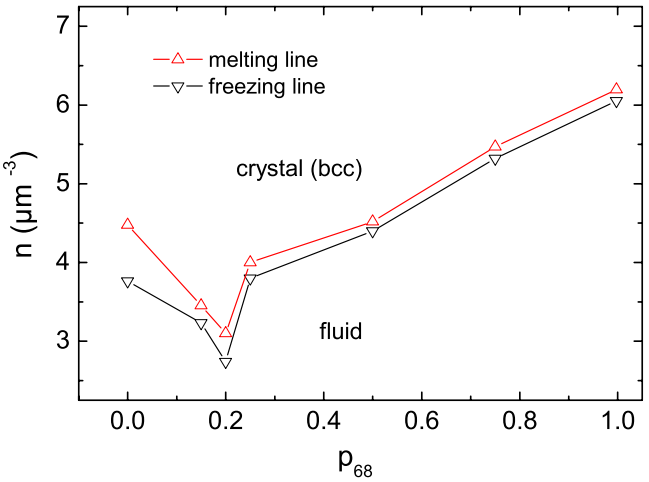

FIG. 2. (Color online) Phase diagram of the *PnBAPS68/PS100B* mixture as obtained from microscopy in the n-p plane. Shown are the freezing line (down triangles) and the melting line (up triangles). The residual uncertainty in n and in p_{68} is of symbol size. At a composition of $p^* \approx 0.2$ the solid-fluid phase transition is shifted to significantly smaller particle number densities revealing an enhanced crystal stability.

point. We therefore observe substitutionally ordered bcc crystals.

For $n \geq 20$ μm^{-3} the full width at half height Δq of the {110}-peak in static light scattering could be evaluated for the average crystallite size L of homogeneously nucleated bulk crystals. Results are displayed in Figs. 4(a) and 4(b). Although in all cases polycrystalline bcc solids are formed, a complex development of the average grain size is observed in dependence on n and p. At low n a shallow minimum in the crystallite size is seen with the smallest crystallites found between $p=0.1$ and $p=0.5$. Beginning at $n=25$ μm^{-3} a maximum appears at $p \approx 0.2$ which becomes more pronounced with increased n. This is highlighted in Fig. 4(b), where we plot L as a function of p for five selected number densities.

B. Elasticity

In Fig. 5(a) we show a three-dimensional (3D) representation of shear moduli as a function of p and n. At constant p G increases with n. At constant n the values at $p=0$ are larger than at $p=1$ due to the larger particle interaction of the PS100B particles. The decrease between these values is nonmonotonous, with a maximum appearing at larger n for $p=0.2-0.3$. This is highlighted in Fig. 5(b) where we compare the experimental composition dependence to the expectation for a random orientation polycrystalline bcc substitutional alloy for five representative n. Within experimental error the model describes the data at lower n. Deviation toward larger than expected values become significant for $0.1 < p_{68} < 0.4$ and $n \geq 30$ μm^{-3}. The maximum deviations are on the order of 10%.

The deviations observed are much smaller than expected for complete demixing or compound formation [29,32]. Moderate deviations have previously observed in a single component system at very large n [71]. That sample showed an increase of grain boundary material as the crystallite size vanished with increased n. As the overall amorphous state was reached, the orientational averaging factor was close to the value expected for homogeneously distributed stress of $f=0.6$. A slight increase of G above the expectations was also seen in a binary mixture at $\Gamma=\Lambda=0.9$ and $n=20$ μm^{-3} [39]. The increase was roughly symmetric with respect to $p=0.5$, while the crystallite size showed no dependence on p. It was attributed to the occurrence of strain due to the misfit of the added minority component. For completeness we note that alternative to structural explanations, the deviations could in principle also indicate an increased effective interaction. The origin of the observed anomaly therefore remains unresolved.

C. Growth velocities

Between freezing and melting the coexisting fluid and crystal densities have to be adjusted by a diffusion process. Therefore we expect a transport limited growth with the

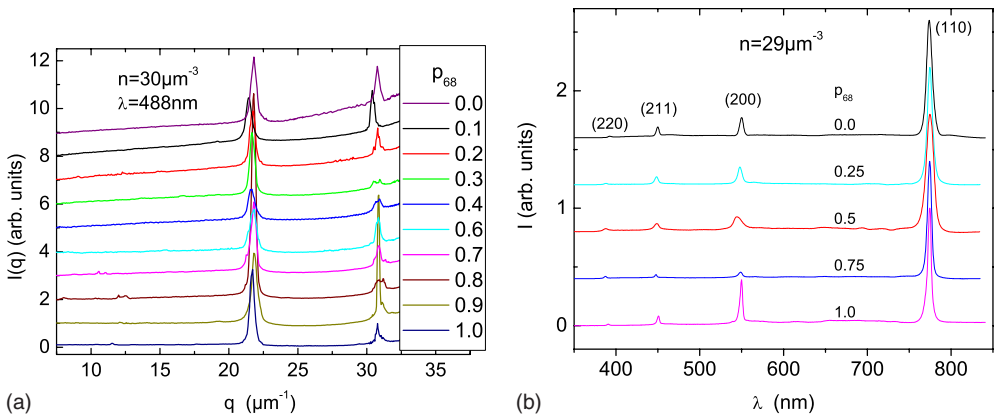

FIG. 3. (Color online) (a) Bragg scattering patterns from static light scattering on homogeneous nucleated powder samples. Data were taken for mixtures of fixed number density $n=30$ μm^{-3} and varied composition as indicated. In all cases a bcc structure is observed with no indications of compound formation at this n. (b) Additional scattering patterns depending on the wavelength of selected mixtures taken with reflection spectroscopy confirming that the mixtures do crystallize in a bcc structure.

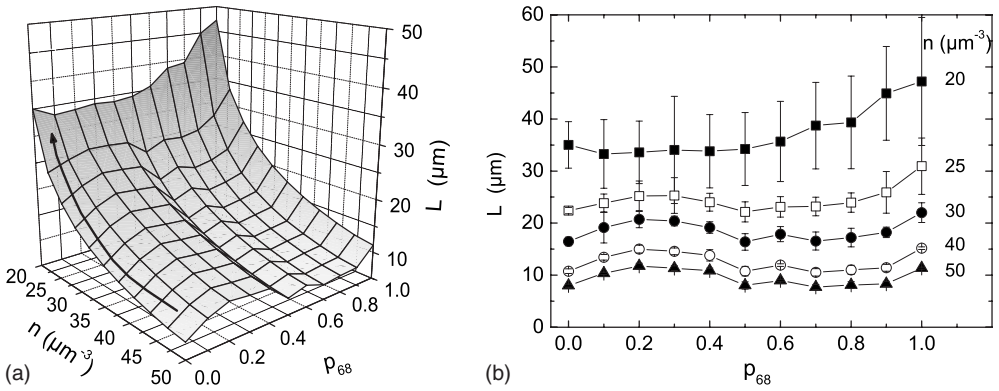

FIG. 4. (a) 3D plot of the average crystallite size as a function of n and p. The arrow marks the direction of dilution of the system. Every crossing point in the wire gauze of the shown surface represents a data point. (b) Composition dependent data for five representative number densities as indicated. Error bars denote the statistical uncertainty. With increased particle concentration the shallow and broad minimum around $p \approx 0.2$ in crystallite size turns to a narrower maximum.

crystal extension increasing with the square root of time. Above coexistence the melt and the evolving solid have the same particle number density. In the absence of segregation processes, growth should therefore be reaction controlled. In Fig. 6(a) we show a double logarithmic plot of the growth curves of heterogeneous nucleated wall crystals obtained for the mixture at $p_{68}=0.2$. The three right curves taken at coexistence indeed show a power law increase with an exponent of 1/2. The apparent deviation from linear growth at short times for $n=3.5\ \mu\text{m}^{-3}$ relates to the fact that the crystal growth starts from a shear induced layer of finite thickness [57]. The curve for $n=8.67\ \mu\text{m}^{-3}$ shows an early cessation of growth upon intersection with bulk nucleated crystals. Otherwise, all curves taken above coexistence for this and all other compositions show a strictly linear, reaction controlled growth.

For the growth curves taken at coexistence we obtain the initial growth velocity from a fit to the first data points in a linear plot. For all other curves linear fits to the complete data set were used. The resulting growth velocities are displayed in Fig. 6(b). Across coexistence the initial growth velocities remain small. Above coexistence all samples show a pronounced increase of growth velocities with increasing n and a saturation at large n. The solid lines represent fits of the Wilson Frenkel growth law of Eq. (6). In all cases the n dependence is well fitted by the theoretical expectation for reaction controlled growth.

Figure 6(c) shows the composition dependence of the velocities for selected number densities. These data were taken from the fits in Fig. 6(b). An interesting behavior is observed. At low number densities a clear maximum is observed at $p=0.2$. This composition corresponds to the minimum of the freezing density. At fixed n the dimensionless under cooling $\Delta\mu$ is largest for this composition. The increased velocity therefore reflects the shape of the phase boundary. At larger densities, however, and in particular for the limiting densities one notices that the maximum still remains, while the values at $n=0.5$ and $n=0.75$ are *below* a straight line connecting the pure component values. A decreased limiting velocity has recently been observed in a mixture of size ratio $\Gamma=0.64$ [72]. It there was attributed to a decreased interfacial thickness caused by a disturbed interfacial layering in the case of mixtures. On the other side the local maximum in the limiting growth velocity is unexpected, except one assumes a

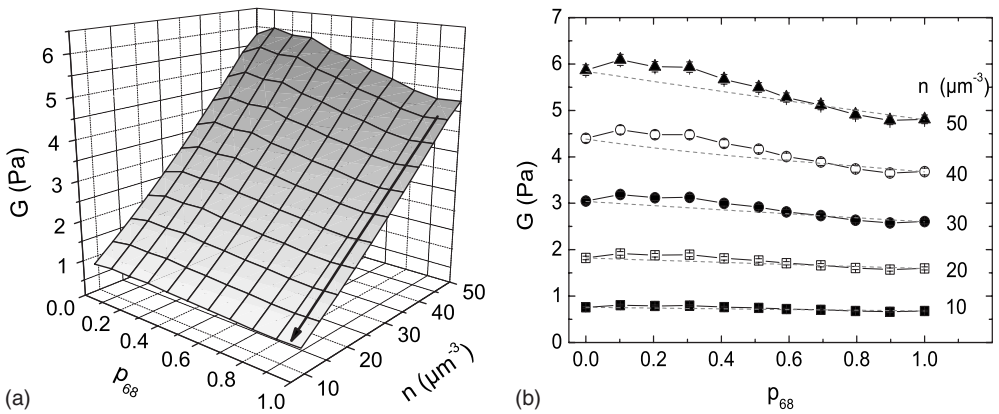

FIG. 5. (a) 3D plot of the shear modulus G as a function of n and p of *PnBAPS68*. The arrow marks the direction of dilution of the system. Every crossing point in the wire gauze of the shown conductivity surface represents a data point. (b) Comparison of experimental data for representative number densities to expectations based on the model for random orientation polycrystalline substitutional alloys fitted to the pure component data (dashed lines). Deviations to larger than expected values are seen on the *PS100B* rich side at larger n.

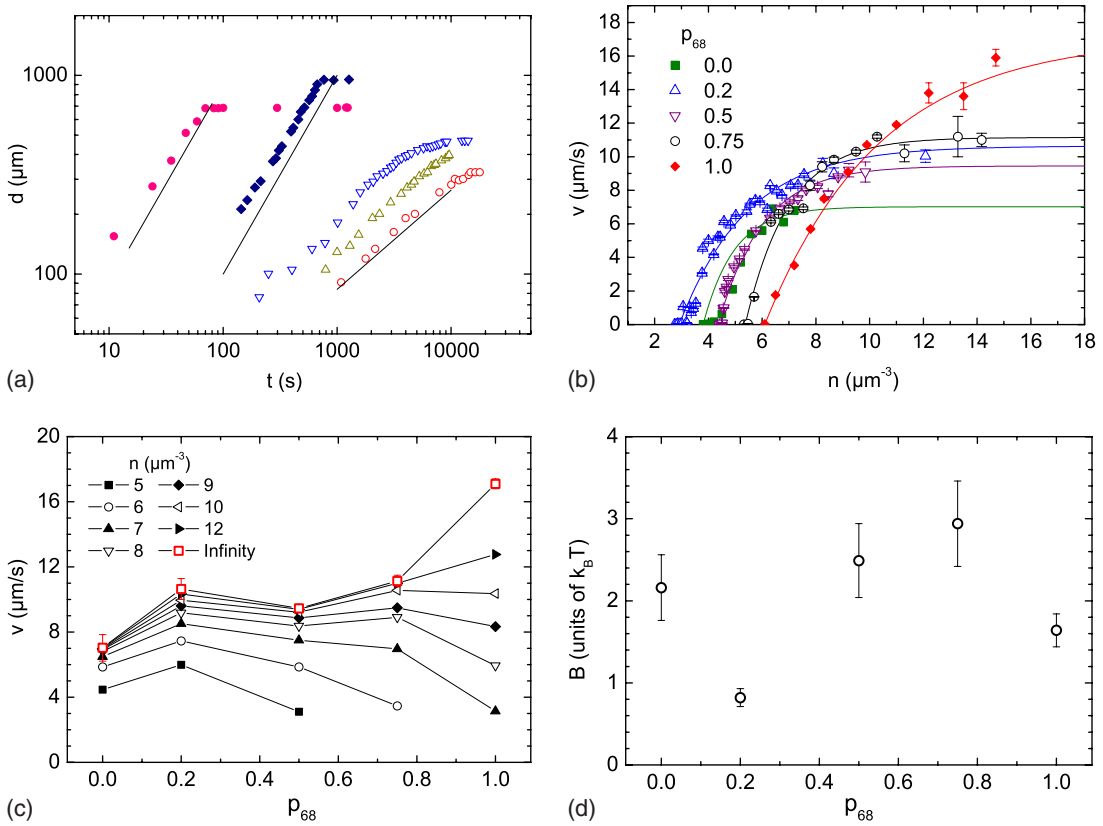

FIG. 6. (Color online) (a) double logarithmic plot of wall crystal growth curves at $p=0.2$ and different n. From left to right: $n=8.7\ \mu\mathrm{m}^{-3}$; $n=3.5\ \mu\mathrm{m}^{-3}$; $n=3.2\ \mu\mathrm{m}^{-3}$; $n=3.0\ \mu\mathrm{m}^{-3}$; and $n=2.95\ \mu\mathrm{m}^{-3}$. The solid lines are guide to the eyes showing power laws of t^1 (left and middle) and $t^{1/2}$ (right). (b) Growth velocities for different p as indicated and as a function of n. Solid lines are fits of Eq. (6) using Würth´s estimate for $\Delta\mu$. (c) Growth velocities as a function of composition p, taken from the fits shown in (b) for different n as indicated. The open squares denote the limiting velocity. (d) Conversion factor B as taken from the fits in (b) as a function of composition p.

widened interface at this particular composition, possibly combined with an enhanced preordering in the adjacent melt.

Figure 6(d) shows the values of the conversion factors B obtained from the Wilson Frenkel fits. Most values are on the order of 2, the value for pure *PnBAPS68* is somewhat lower but $B(p^*)=0.82$ only. Compared to other p, the limiting velocity is approached much slower with increased n for this composition. On the other side at a given large n the chemical potential difference between melt and solid or the dimensionless under cooling is much smaller for p^* than for the other compositions. Playing with Eq. (3) shows that the interaction strength does not vary much as a function of composition. However, the reduced B value may be rationalized, if we assume the melt structure to be much closer to that of the formed solid than for the other compositions. Then for both phases the chemical potential remains more similar.

D. Nucleation kinetics

Finally, using Avrami´s model of solidification, we combine the average crystallite size obtained from static light scattering with the limiting velocities from microscopy to obtain the average nucleation rate density J.

Figure 7(a) shows the composition dependence of the nucleation rate density, which also displays an anomalous behavior at a composition of $p^*=0.2$. At the lowest $n=20\ \mu\mathrm{m}^{-3}$ the rate density is the largest one while it is the smallest at the highest investigated $n=50\ \mu\mathrm{m}^{-3}$. In Fig. 7(b) we show the results in dependence on n for compositions of $p\in\{0;0.2;0.5;0.75;1\}$. In all cases a steep but slowing increase of J over about two orders of magnitude with n increasing from 20 to 50 $\mu\mathrm{m}^{-3}$ is observed. The mixture at $p^*=0.2$ deviates from the others showing the smallest increase, crossing all other curves.

A strong but sublinear increase of the nucleation rate density in a semilogarithmic plot of J versus n has already been observed in several single component systems [39,73] and in a mixture at $p=0.5$ [39]. For the case pure PnBAPS68 it was quantitatively interpreted in the framework of classical nucleation theory (CNT) [73]. CNT suggests that nucleation is an activated process of rate density $J(n,p)=J_0(n,p)\exp[-\Delta G^*(n,p)/k_BT]$ where $J_0(n,p)$ is a kinetic prefactor and $\Delta G^*(n,p)=(16\pi/3)\gamma(n,p)^3/[n\Delta\mu(n,p)]^2$ is the barrier height for nucleation. Both the surface tension $\gamma(n,p)$ and the under cooling $\Delta\mu(n,p)$ depend on the particle number density n and the composition p [27,72,74].

Taking $\Delta\mu(n,p)$ from the growth measurements [Fig. 8(a)] we may check for $\gamma(n,p)$ by plotting for each p the natural logarithm of the measured J versus $1/(n\Delta\mu)^2$ [73]. The under cooling is given as $\Delta\mu=B\Pi^*$. At very low n close

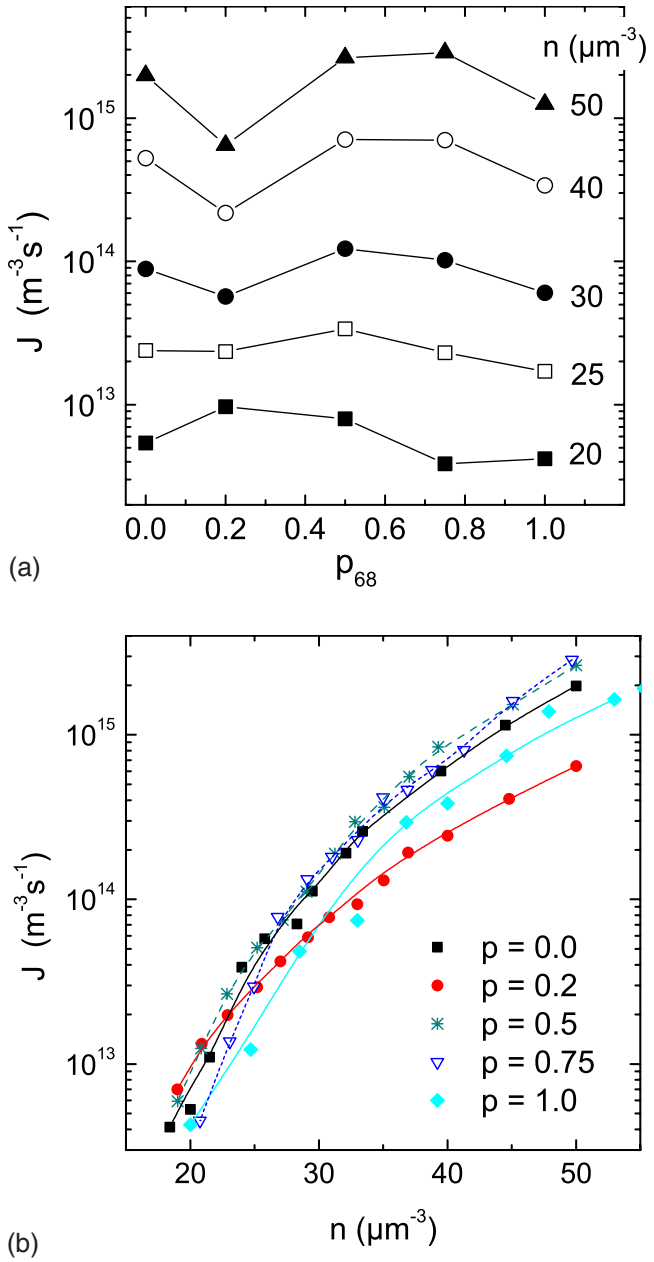

FIG. 7. (Color online) (a) Composition dependence of the homogeneous nucleation rate densities for representative number densities. (b) Nucleation rate densities J in dependence on particle number density n and number fraction p. Data were determined from the average crystallite sizes (Fig. 3) and the limiting growth velocities [Fig. 6(c)] using the Avrami model. The lines are guides to the eyes.

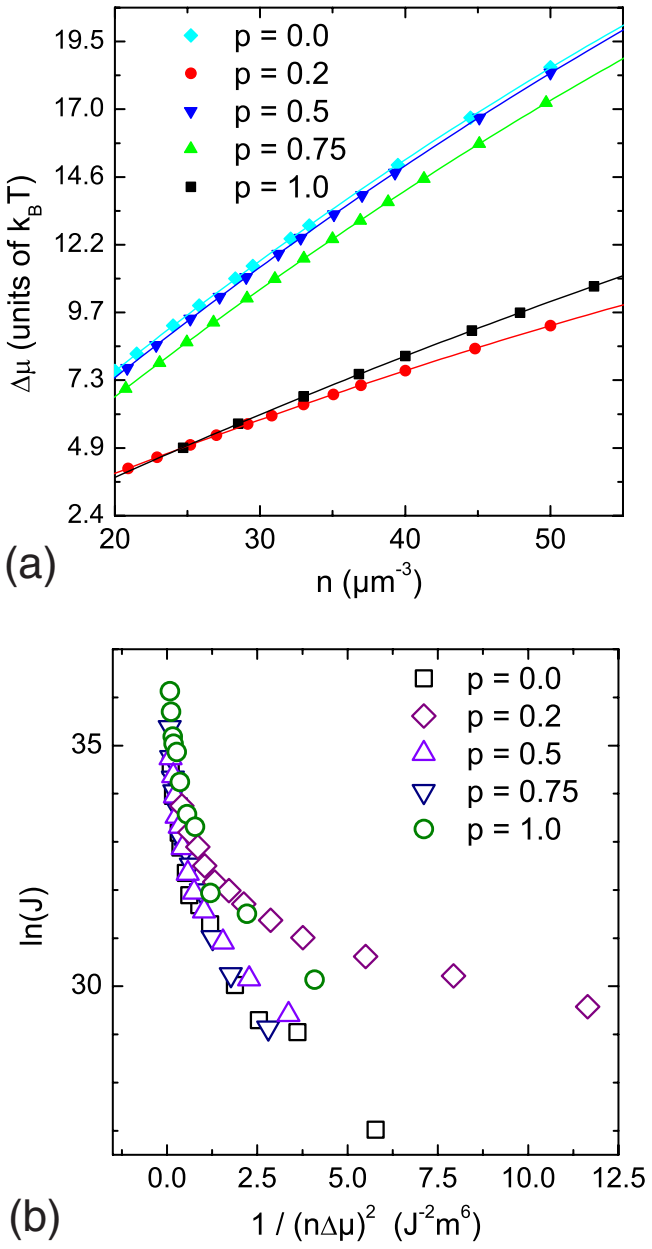

FIG. 8. (Color online) (a) Chemical potential difference between melt and solid as function of particle number density for different compositions as indicated. (b) Natural logarithm of the measured nucleation rate densities is plotted versus $(n\Delta\mu)^{-2}$ for different compositions as indicated. This allows for a qualitative estimate for the density and composition dependence of the surface tension γ.

to the phase boundary the chemical potential difference is dominated by the composition dependence of the relative distances to the phase boundary $[n\text{-}n_F(p)]/n_F(p)$. With increasing n this factor loses importance and for sufficiently large n the chemical potential difference is approximately $\Delta\mu(p) \propto n\ B(p)$. This applies to the concentration range the nucleation rate densities were determined. An estimate of the density and composition dependence of $\gamma(n,p)$ may be obtained from Fig. 8(b). At each point of the curves the local slope is proportional to γ^3. Clearly all curves are steep at large under cooling (large n) indicating a large and nearly composition independent surface tension. Hence within CNT, for all compositions the slowing increase of the nucleation rate density with n can be assigned to an increased surface tension [73]. Only at small under cooling (lower n) a composition dependence is evident. In particular the curve for p^*=0.2 shows a significantly lower slope corresponding to a lower surface tension for that composition. This points to a structural similarity between crystal and melt phase at low n.

IV. DISCUSSION

It is instructive to first summarize our experimental observations. For a de-ionized colloidal charged sphere mixture of $\Gamma=0.68$ and $\Lambda\cong 1$ we observed a pronounced stability of the crystal phase at a composition of $p=0.1-0.3$ with a rather sharp peak at $p^*=0.2$. Structure analysis gave no evidence of compound formation. We applied a highly reproducible sample conditioning technique with control of de-ionization, composition, and density by combined light scattering and conductivity experiments. By this we were able to restrict the preparational uncertainties sufficiently to facilitate systematic measurements of several properties in the crystalline phase at identical conditions and compare these to expectations based on a simple theoretical model. We observed correlated deviations in the crystallite size, the elasticity, the growth velocity, the n dependence of the under cooling and the nucleation rate density, which are small in magnitude but significant within the remaining experimental uncertainty.

It is interesting to contrast our findings on the phase behavior to those made on other systems. First, our results differ from previous observations on and calculations for binary colloidal mixtures, as here for the first time at a certain composition the crystal stability is enhanced, even above that observed for the pure components. The underlying reason for the enhanced stability of the crystalline phase at $p^*=0.2$ is not known in detail. It is, however, striking that no stability maximum was observed in other mixtures, where $\Gamma\cong\Lambda<1$ [34,36] while it is observed here, where $\Gamma<\Lambda\cong 1$.

Second, in the context of atomic phase diagrams a locally enhanced stability about a p corresponding to a stoichiometric compound is rather common and in particular for strongly covalent interactions the compound often displays the global stability maximum [75]. Directed interactions as well as favorable geometrical packing have been discussed as underlying reasons [42]. Also in hard sphere colloids, compound formation due to favorable packing is frequent and may lead to a stability maximum, if the interactions are nonadditive [25].

In the present charged sphere mixture, compound formation (e.g., of bcc Fe_3Al type [76]) can be excluded as origin of the stability maximum from the structural analysis at $n=30\ \mu m^{-3}$. In a way, its absence may even be expected. Okubo had suggested to use an effective size ratio, where the sphere radii are replaced by effective radii $a_{eff}=a+\kappa^{-1}$ [31]. In our case $a_{eff,S}=217$ nm and $a_{eff,L}=244$ nm, yielding $\Gamma_{eff}=0.89$. This should be compared to recent Monte Carlo simulations on binary hard spheres, where at $\Gamma=0.92$ at $p=0.23$ a (lower) azeotrope with substitutionally ordered crystals in the solid was observed [25]. Combined with previous observations [31–33] our findings suggest that compounds form in colloidal systems only for sufficiently short-ranged repulsions and low size ratios. At long-ranged repulsions the resulting packing advantages are too weak to govern compositional order and substitutional alloys are formed.

Third, in atomic and molecular systems also upper azeotropes present stability maxima, but these are less frequent than compounds. They occasionally occur as local maxima, e.g., in γ-AlMg or bcc AgMg or as global maxima, e.g., in AlMn [75]. For hard sphere systems upper azeotropes have neither been predicted nor observed. An upper azeotrope is usually discussed in terms of miscibility. At the azeotropic composition p^* the miscibility of the system should be larger in the crystalline phase than in the corresponding melt. It is, however, not immediately obvious, how to apply and quantify this concept in the present case.

We observed that at p^* the chemical potential of the crystal phase and the corresponding melt equal at lower n than for other compositions. At the same time this is coupled to a lowered conversion factor B, which implies a more similar n dependence of the chemical potential for both phases above n_F than for the adjacent compositions and thus a smaller slope of the chemical potential versus n. In addition, the limiting velocity at p^* is increased, while the surface tension between melt and solid $\gamma(p^*)$ is considerably lower. Together this possibly indicates a structure for the fluid and the melt which at p^* is closer to that of the corresponding solid than for the other compositions. It would therefore be particularly interesting to study the melt structure in comparison to that of the solid [77]. This will allow to check our suggestion and possibly access a microscopic foundation of our observations.

Alternatively to structural arguments, one may consider possible changes in the interactions between large and small spheres. Starting from earlier observations on mixtures at large size and charge ratio, we here have assumed that the interactions also for the present mixture are well approximated using number weighted averages. If, for some reason (e.g., connected to many body terms in the effective interaction), at p^* the repulsion would be less screened or shielded, a decreased freezing density would be the immediate consequence. Refined knowledge of the effective interaction potential in de-ionized charged sphere mixtures is therefore eagerly awaited. First steps in that direction have been taken [65,66], future studies might also consider mixtures of low Γ and large Λ.

Finally, the enhanced crystal stability is also correlated with some peculiarities observed in the solidification kinetics. At low n both v and J show maximum values at about p^*. The growth velocity gets independent of n for large particle densities and shows a local maximum at p^*. The nucleation rate density, however continues to increase with n. The composition dependence of J is dominated by the composition dependence of the barrier height for nucleation, which is the smallest at p^*. This was here shown for a particular mixture showing an specific type of phase diagram. It may, however bear some more general implication also for other types of phase diagrams. It would for instance be interesting to apply the same analysis to the composition dependence of solidification in a eutectic mixture. One may argue that our results at this point depend on the applicability and correctness of CNT which still lacks a rigorous theoretical connection between realistic microscopic mechanisms and macroscopic thermodynamic quantities [27,73]. Staying qualitative however, CNT offers the advantage, that the only assumptions involved are the existence of an attempt frequency and of an activated process.

V. CONCLUSIONS

We have studied the phase behavior and crystallization kinetics of a binary charged sphere mixture under conditions

of very long-ranged repulsions. In particular we investigated two particle species of moderately different size but very similar effective charge. The present study added a previously unobserved type of phase diagram to the richness of colloidal phase behavior: an upper azeotrope. By careful adjustment and control of the system parameters small but significant correlations between several properties of the mixtures were detected. In particular, we provide a first database for the combined composition and density dependence of crystallization kinetics in a mixture with small charge ratio and large size ratio. The amount and quality of gathered data allowed a systematic comparison to other system classes as well as a discussion of possible underlying reasons for the observed enhanced crystal stability and the superior miscibility in the crystalline phase. A number of future experiments were suggested. In addition, however, we hope to have attracted further theoretical attention to the effective interactions, the phase behavior and the phase transition kinetics of binary charged sphere mixtures.

ACKNOWLEDGMENTS

We are indebted to J. Liu for providing the microscopy data. We further like to thank N. Lorenz and H. Löwen for many interesting discussions on alloy formation and the BASF AG (Ludwigshafen, Germany) for their kind gift of particles. This work was financially supported by the Deutsche Forschungsgemeinschaft (Grants No. Pa459/14-16, No. He1601/23, and No. He1601/24), and the Materialwissenschafliches Forschungszentrum (MWFZ) Mainz. This is gratefully acknowledged.

[1] P. N. Pusey, in *Liquids, Freezing and Glass Transition*, Ecole d'été, Les Houches Vol. 51, edited by J. P. Hansen, D. Levesque, and J. Zinn-Justin (Elsevier, Amsterdam, 1991), p. 763.
[2] A. K. Sood, in *Solid State Phys.*, edited by H. Ehrenreich and D. Turnbull (Academic, New York, 1991), Vol. 45, p. 1.
[3] V. J. Anderson and H. N. W. Lekkerkerker, Nature (London) **416**, 811 (2002).
[4] B. J. Ackerson, Phase Transit. **21**, 73 (1990).
[5] T. Palberg, J. Phys.: Condens. Matter **11**, R323 (1999).
[6] M. D. Elliot and W. C. K. Poon, Adv. Colloid Interface Sci. **92**, 133 (2001).
[7] H. Löwen, Phys. Rep. **237**, 249 (1994).
[8] R. van Roij and R. Evans, J. Phys.: Condens. Matter **11**, 10047 (1999).
[9] J. V. Sanders and M. J. Murray, Nature (London) **275**, 201 (1978).
[10] J. V. Sanders, Philos. Mag. A **42**, 705 (1980).
[11] S. Hachisu and S. Yoshimura, Nature (London) **283**, 188 (1980).
[12] H. M. Lindsay and P. M. Chaikin, J. Chem. Phys. **76**, 3774 (1982).
[13] P. Bartlett, R. H. Ottewill, and P. N. Pusey, J. Chem. Phys. **93**, 1299 (1990).
[14] P. Bartlett, R. H. Ottewill, and P. N. Pusey, Phys. Rev. Lett. **68**, 3801 (1992).
[15] P. Bartlett and P. N. Pusey, Physica A **194**, 415 (1993).
[16] W. J. Hunt, R. Jardine, and P. Bartlett, Phys. Rev. E **62**, 900 (2000).
[17] A. B. Schofield, Phys. Rev. E **64**, 051403 (2001).
[18] A. B. Schofield, P. N. Pusey, and P. Radcliffe, Phys. Rev. E **72**, 031407 (2005).
[19] F. X. Redl, K. S. Cho, C. B. Murray, and S. O'Brien, Nature (London) **423**, 968 (2003).
[20] P. Bartlett, J. Phys.: Condens. Matter **2**, 4979 (1990).
[21] X. Cottin and P. A. Monson, J. Chem. Phys. **102**, 3354 (1995).
[22] G. Jackson, J. S. Rowlinson, and F. B. van Swol, J. Phys. Chem. **91**, 4907 (1987).
[23] X. C. Zeng and D. W. Oxtoby, J. Phys. Chem. **93**, 4357 (1990).
[24] M. D. Eldridge, P. A. Madden, and D. Frenkel, Nature (London) **365**, 35 (1993).
[25] S. Punnathanam and P. A. Monson, J. Chem. Phys. **125**, 024508 (2006).
[26] H. Xu and M. Baus, J. Phys. Chem. **118**, 5045 (2003).
[27] R. P. Sear, J. Phys.: Condens. Matter **19**, 033101 (2007).
[28] P. M. Chaikin, J. M. diMeglio, W. Dozier, H. M. Lindsay, and D. A. Weitz, in *Physics of Complex and Supramolecular Fluids*, edited by S. A. Safran and N. A. Clark (Wiley-Interscience, New York, 1987), pp 65.
[29] W. J. Hunt and C. F. Zukoski, J. Colloid Interface Sci. **210**, 332 (1999).
[30] P. D. Kaplan, J. L. Rouke, A. G. Yodh, and D. J. Pine, Phys. Rev. Lett. **72**, 582 (1994).
[31] T. Okubo, J. Chem. Phys. **93**, 8276 (1990).
[32] L. Liu, S. Xu, J. Liu, and Zh. Sun, J. Colloid Interface Sci. **326**, 261 (2008).
[33] T. Okubo and H. Ishiki, Colloid Polym. Sci. **279**, 571 (2001).
[34] A. Meller and J. Stavans, Phys. Rev. Lett. **68**, 3646 (1992).
[35] N. Lorenz, H. J. Schöpe, and T. Palberg, J. Chem. Phys. (to be published).
[36] T. Okubo and H. Fujita, Colloid Polym. Sci. **274**, 368 (1996).
[37] P. Wette, H. J. Schöpe, and T. Palberg, Prog. Colloid Polym. Sci. **118**, 260 (2001).
[38] P. Wette, H. J. Schöpe, R. Biehl, and T. Palberg, J. Chem. Phys. **114**, 7556 (2001).
[39] P. Wette, H. J. Schöpe, T. Palberg, J. Chem. Phys. **122**, 144901, (2005).
[40] N. Lorenz, P. Wette, H. J. Schöpe, and T. Palberg, Philos. Mag. (to be published).
[41] N. Lorenz, H. J. Schöpe, H. Reiber, T. Palberg, I. Klassen, P. Wette, I. Klassen, D. Holland-Moritz, D. Herlach, and T. Okubo, J. Phys.: Condens. Matter (to be published).
[42] T. B. Massalski, in *Physical Metallurgy*, edited by W. Cahn and P. Haasen (North Holland, Amsterdam, 1996), Vol. 1, Chap. 3, p. 135.
[43] R. Klein, H. H. v. Grünberg, C. Bechinger, M. Brunner, and V. Lobashkin, J. Phys.: Condens. Matter **14**, 7631 (2002).

[44] Y. Levin, Rep. Prog. Phys. **65**, 1577 (2002).
[45] S. Alexander, P. M. Chaikin, P. Grant, G. J. Morales, P. Pincus, and D. Hone, J. Chem. Phys. **80**, 5776 (1984).
[46] L. Belloni, Colloids Surf., A **140**, 227 (1998).
[47] E. Trizac and Y. Levin, Phys. Rev. E **69**, 031403 (2004).
[48] T. Kreer, J. Horbach, and A. Chatterji, Phys. Rev. E **74**, 021401 (2006).
[49] P. Wette, H. J. Schöpe, and T. Palberg, Colloids Surf., A **222**, 311 (2003).
[50] L. Shapran, M. Medebach, P. Wette, H. J. Schöpe, T. Palberg, J. Horbach, T. Kreer, and A. Chaterji, Colloids Surf., A **270-271**, 220 (2005).
[51] L. Shapran, H. J. Schöpe, and T. Palberg, J. Chem. Phys. **125**, 194714 (2006).
[52] P. Wette and H. J. Schöpe, Prog. Colloid Polym. Sci. **133**, 88 (2006).
[53] M. Medebach and T. Palberg, J. Phys.: Condens. Matter **16**, 5653 (2004).
[54] H. J. Schöpe and T. Palberg, J. Colloid Interface Sci. **234**, 149 (2001).
[55] D. Hessinger, M. Evers, and T. Palberg, Phys. Rev. E **61**, 5493 (2000).
[56] M. Medebach, R. Chuliá Jordán, H. Reiber, H. J. Schöpe, R. Biehl, M. Evers, D. Hessinger, J. Olah, T. Palberg, E. Schönberger, and P. Wette, J. Chem. Phys. **123**, 104903 (2005).
[57] A. Stipp, R. Biehl, Th. Preis, J. Liu, A. Barreira Fontecha, H. J. Schöpe, and T. Palberg, J. Phys.: Condens. Matter **16**, S3885 (2004).
[58] H. J. Schöpe, Th. Decker, and T. Palberg, J. Chem. Phys. **109**, 10068 (1998).
[59] M. Würth, J. Schwarz, F. Culis, P. Leiderer, and T. Palberg, Phys. Rev. E **52**, 6415 (1995).
[60] T. Palberg, H. Hecht, E. Simnacher, T. Loga, F. Falcoz, J. Kottal, and P. Leiderer, J. Phys. (France) **4**, 31 (1994).
[61] Y. Monovoukas, G. G. Fuller, and A. P. Gast, J. Chem. Phys. **93**, 8294 (1990).
[62] A. Reuss, Z. Angew. Math. Mech. **9**, 49 (1929).
[63] H. Reiss, J. Chem. Phys. **18**, 840 (1950).
[64] R. Hill, Proc. Phys. Soc., London, Sect. A **65**, 349 (1952).
[65] A. Torres, G. Tennes, and R. van Roij, J. Chem. Phys. **128**, 154906 (2008).
[66] A. Torres, A. Cuetos, M. Dijkstra, and R. van Roij, Phys. Rev. E **77**, 031402 (2008).
[67] D. J. W. Aastuen, N. A. Clark, L. K. Cotter, and B. J. Ackerson, Phys. Rev. Lett. **57**, 1733 (1986); **57**, 2772(E) (1986).
[68] J. Liu and T. Palberg, Prog. Colloid Polym. Sci. **123**, 222 (2004).
[69] J. L. Langford and A. J. C. Wilson, J. Appl. Crystallogr. **11**, 102 (1978).
[70] M. Avrami, J. Chem. Phys. **7**, 1103 (1939); **8**, 212 (1940); **9**, 177 (1941).
[71] H. J. Schöpe and T. Palberg, J. Non-Cryst. Solids **307–310**, 613 (2002).
[72] A. Stipp and T. Palberg, Philos. Mag. **87**, 899 (2007).
[73] P. Wette and H. J. Schöpe, Phys. Rev. E **75**, 051405 (2007).
[74] C. V. Thompson and F. Spaepen, Acta Metall. **31**, 2021 (1983).
[75] *Binary Alloy Phase Diagrams*, 2nd ed., edited by B. Massalski and H. Okamoto (ASM International, Materials Park, Ohio, 1990); see also http://www.crct.polymtl.ca/FACT/.
[76] C. Mocuta, H. Reichert, K. Mecke, H. Dosch, and M. Drakopoulos, Science **308**, 1287 (2005).
[77] P. Wette, I. Klassen, D. Holland-Moritz, T. Palberg, S. V. Roth, and D. M. Herlach, Phys. Rev. E **79**, 010501(R) (2009).